

# Calculating the millimetre-wave scattering phase function of snowflakes using the self-similar Rayleigh–Gans Approximation

Robin J. Hogan,<sup>a\*</sup> Ryan Honeyager,<sup>b</sup> Jani Tyynelä<sup>c</sup> and Stefan Kneifel<sup>d</sup>

<sup>a</sup>European Centre for Medium Range Weather Forecasts, Reading, UK

<sup>b</sup>Department of Earth, Ocean and Atmospheric Science, Florida State University, Tallahassee, USA

<sup>c</sup>Finnish Meteorological Institute, Helsinki, Finland

<sup>d</sup>Institute for Geophysics and Meteorology, University of Cologne, Germany

\*Correspondence to: R. J. Hogan, ECMWF, Shinfield Park, Reading RG2 9AX, UK.

E-mail: r.j.hogan@ecmwf.int

Exploitation of millimetre-wave radiometer and radar observations of ice clouds and snow requires the ability to model the scattering properties of snowflakes. This article extends the Self-Similar Rayleigh–Gans Approximation (SSRGA) for rapid computation of the backscatter cross-section of ice aggregates, to compute the full scattering phase function, the scattering and absorption cross-sections and the asymmetry factor. We also show that the Rayleigh–Gans Approximation (RGA) may be improved to represent the enhanced scattering and absorption when the monomers from which the aggregate is composed are non-spherical. The new model is shown to perform well when compared to benchmark 94 and 183 GHz Discrete Dipole Approximation (DDA) calculations of the scattering by simulated unrimed aggregates of maximum dimension up to 1 cm that have a mass–size relationship in the range observed from aircraft. For denser particles, such as would result from riming, the validity of the underlying RGA becomes questionable and both the backscatter and scattering cross-sections can be underestimated by a factor of 2.

**Key Words:** Rayleigh–Gans approximation; discrete dipole approximation; scattering phase function; snowflakes; aggregation; millimetre-wave radar

Received 15 June 2016; Revised 1 November 2016; Accepted 9 November 2016; Published online in Wiley Online Library

## 1. Introduction

Recent years have seen increasing use of both passive and active millimetre-wave observations of ice clouds and snow from space. Cloud-affected millimetre-wave radiometer observations with frequencies up to 183 GHz are shortly to be operationally assimilated into a numerical weather prediction (NWP) model (Geer *et al.*, 2014), with sub-millimetre instruments under active consideration for future deployment (e.g. Buehler *et al.*, 2007). In terms of active observations, the 94 GHz CloudSat radar has been used to evaluate ice clouds and snow in NWP models (Delanoë *et al.*, 2011) and has been assimilated into models (Janisková *et al.*, 2012). Such measurements will be continued with the Dopplerized 94 GHz radar on the forthcoming EarthCARE satellite (Illingworth *et al.*, 2015). Radars with frequencies up to 220 GHz have been proposed for future ground-based and satellite deployment (Hogan and Illingworth, 1999; Battaglia *et al.*, 2014).

Correct interpretation of such measurements in a variational retrieval or data assimilation scheme requires a fast ‘forward model’ which takes as input a profile of estimated atmospheric properties, and predicts the corresponding radiance or apparent radar reflectivity. Strong scattering of millimetre wavelengths by ice particles means that a good estimate of their scattering cross-section is required, along with a measure of the preference for

forward over backward scattering. For example, the ‘RTTOV-SCATT’\* radiance model (Bauer *et al.*, 2006), used in operational data assimilation, characterizes the scattering pattern by the fraction of scattered radiation that is in the backward hemisphere. The multi-sensor cloud and precipitation retrieval algorithm for EarthCARE (Illingworth *et al.*, 2015) represents radar multiple scattering with the Hogan and Battaglia (2008) model, which characterizes the scattering pattern by the asymmetry factor  $g$ , equal to the average of the cosine of the scattering angle.

The state-of-the-art approach to estimate the scattering properties of snowflakes is to apply the Discrete Dipole Approximation (DDA; Draine and Flatau, 1994) to a large number of realistic 3D particles, but this is very computationally costly. For the radar backscatter problem, much cheaper alternatives exist. For particles no larger in size than the wavelength of the radiation, Matrosov *et al.* (2005) and Hogan *et al.* (2012) demonstrated that they may be treated as oblate, horizontally oriented ‘soft spheroids’ with an aspect ratio of around 0.6, composed of a homogeneous mixture of ice and air. For larger ice particles the internal structure becomes important, and soft spheres or spheroids give an increasingly poor estimate of the scattering

\*RTTOV = Radiative Transfer model for TIROS Operational Vertical Sounder.

properties as the particles get larger (e.g. Petty and Huang, 2010; Tyynelä *et al.*, 2011; Geer and Baordo, 2014). However, since the density of large aggregates is low, the Rayleigh–Gans Approximation (RGA) has been found to be valid (Matrosov, 1992; Westbrook *et al.*, 2006; Tyynelä *et al.*, 2013; Leinonen *et al.*, 2013). In this approximation, the electric field experienced at any point in the particle is approximated by the incident field, thereby neglecting interaction between dipoles. The backscatter cross-section may then be estimated numerically from a 1D description of the structure of the particle in the direction of the incident wave.

Hogan and Westbrook (2014) showed that, for realistic aggregates, this 1D function has a self-similar structure, and hence that its power spectrum can be represented by a power law. They referred to this as the Self-Similar Rayleigh–Gans Approximation (SSRGA). It leads to an analytic function for the average backscatter of an ensemble of particles of a particular size, in which their structure is described by just four parameters: their aspect ratio, a kurtosis parameter describing the extent to which the ice is concentrated in the centre of the particle, and two parameters describing the power law. Hogan and Westbrook (2014) estimated these parameters for snowflakes generated by the aggregate model of Westbrook *et al.* (2004).

In this article, the SSRGA is extended to predict the full scattering pattern of snowflakes at millimetre wavelengths, enabling it to be used in both radar multiple-scattering and radiance models. Section 2 describes the theoretical basis for this extension, including an improvement to the underlying RGA to represent the enhanced scattering and absorption by aggregates composed of non-spherical monomers. In section 3, the five parameters used by the new SSRGA to describe the spatial structure of aggregates are computed for synthetic particles generated by the Westbrook *et al.* (2004) and Nowell *et al.* (2013) models. Then in section 4, the scattering properties predicted by SSRGA are compared to benchmark DDA calculations performed on the same aggregates.

## 2. Theory

### 2.1. The Rayleigh–Gans approximation

The Rayleigh–Gans approximation is applicable when a particle interacts only weakly with the incident radiation such that the electric field experienced at any point in the particle may be approximated by the incident field. Essentially each volume element behaves as an independent Rayleigh scatterer, and the scattered field in any direction may be found by coherently summing the contributions from all volume elements in the particle. For particles whose geometries can be described analytically, this leads to analytic forms for the scattering properties. In the backscatter direction, we write the backscatter cross-section as a modification of Rayleigh scattering:

$$\sigma_b = \frac{9}{4\pi} k^4 |K|^2 V^2 \phi(x), \quad (1)$$

where  $V$  is the volume of the particle (in the case of an ice particle it is the volume of ice excluding air) and  $k = 2\pi/\lambda$  is the wavenumber where  $\lambda$  is the wavelength in vacuum. (Note that (1) gives the ‘radar’ backscatter cross-section with units of  $\text{m}^2$ , but in some conventions there is an extra factor of  $4\pi$  in the denominator to yield cross-section per unit solid angle with units  $\text{m}^{-2} \text{sr}^{-1}$ .) Two terms lead to a deviation from classical Rayleigh theory:

- The term  $\phi(x)$ , where  $x = kD$ , expresses the deviation from Rayleigh scattering due to the particle size in the direction of propagation,  $D$ , no longer being small compared to the wavelength. For small particles,  $\phi \simeq 1$  and (1) reverts to the expression for Rayleigh scattering (e.g. van de Hulst, 1957, section 20.42). When the size of the particle becomes

significant compared to the wavelength, then destructive interference from the nearest and furthest parts of the particle leads to a reduction in the backscatter, and  $\phi$  drops below 1. For ice aggregates, it may be represented using the SSRGA, described in section 2.2.

- The  $K$  term expresses the polarizability of the medium, and traditionally the RGA follows Rayleigh scattering and uses the Claussius–Mossotti factor

$$K_{\text{CM}} = \frac{\epsilon - 1}{\epsilon + 2}, \quad (2)$$

where  $\epsilon$  is the complex dielectric constant of solid ice. However, this formula makes the implicit assumption that the aggregate is composed of spherical monomers. Section 2.3 describes how to compute  $K$  for more realistic non-spherical ice monomers, leading to systematically more scattering and absorption for the same volume of ice; a formula for the absorption cross-section is also provided.

After describing how the modified terms in (1) are derived to get an accurate estimate of the backscatter cross-section, section 2.4 then describes how the full scattering phase function may be computed, and from that the scattering cross-section. Section 2.5 then outlines the limited extent to which SSRGA can predict polarization properties.

### 2.2. The self-similar Rayleigh–Gans approximation

The exact form of  $\phi(x)$  depends on the internal structure of the particle. In the case of ‘soft spheres’ consisting of a homogeneous mixture of ice and air, Eq. 2 of Hogan and Westbrook (2014) can be rearranged to obtain

$$\phi_{\text{sphere}}(x) = 9 \left( \frac{\sin x - x \cos x}{x^3} \right)^2. \quad (3)$$

This expression has minima at regular intervals in  $x$  where the backscattering falls to exactly zero due to perfect destructive interference from different parts of the particle. Only a small modification is required to represent scattering by homogeneous spheroids.

Various studies (e.g. Petty and Huang, 2010; Tyynelä *et al.*, 2011) have found that, for realistic ice particles at millimetre wavelengths, the spherical or spheroidal approximation embodied in (3) underestimates backscatter to an increasing extent as  $x$  increases. This is because real ice particles have structure at all scales, so there is much less destructive interference in the backscatter direction. Hogan and Westbrook (2014) found that the internal structure of irregular ice aggregates could be characterized statistically by three parameters, leading to an expression for the mean backscatter of an ensemble of particles of the same size with statistically similar properties. In the context of (1), this leads to the SSRGA:

$$\begin{aligned} \phi_{\text{SSRGA}}(x) = & \frac{\pi^2}{4} \left[ \cos^2(x) \left\{ \left( 1 + \frac{\kappa}{3} \right) \left( \frac{1}{2x+\pi} - \frac{1}{2x-\pi} \right) \right. \right. \\ & \left. \left. - \kappa \left( \frac{1}{2x+3\pi} - \frac{1}{2x-3\pi} \right) \right\}^2 \right. \\ & \left. + \beta \sin^2(x) \sum_{j=1}^n \zeta_j (2j)^{-\gamma} \right. \\ & \left. \times \left\{ \frac{1}{(2x+2\pi j)^2} + \frac{1}{(2x-2\pi j)^2} \right\} \right]. \quad (4) \end{aligned}$$

The physical interpretation of the three parameters of Hogan and Westbrook (2014) is as follows.

- The kurtosis parameter,  $\kappa$ , describes the mean structure of the particle and specifically the extent to which ice is concentrated toward the centre. Thus a positive value indicates mass concentrated toward the centre with only tenuous outer parts, while a negative value indicates a more uniform distribution.
- The power-law prefactor,  $\beta$ , describes the amplitude of the random fluctuations in structure relative to the amplitude of the mean structure.
- The power-law exponent,  $\gamma$ , describes the extent to which smaller-scale structures in the particle have a smaller amplitude.

Hogan and Westbrook (2014) analyzed realistically simulated aggregates from the Westbrook *et al.* (2004) model to suggest typical values for these numbers. In practice, two further parameters are required in order to apply SSRGA optimally:

- The effective aspect ratio,  $\alpha_{\text{eff}} = D/D_{\text{max}}$  is the ratio of particle size in the direction of propagation,  $D$ , to the maximum dimension of the particle in any direction,  $D_{\text{max}}$ . In the case of horizontally aligned ice aggregates being observed by vertically pointing radar, this becomes the actual aspect ratio  $\alpha$ , and Hogan *et al.* (2012) showed that a value of 0.6 was reasonable. In the case of simulating radiances observed at arbitrary angles, or radar multiple scattering, it is more appropriate to treat the particles as being randomly oriented with respect to the incident radiation, in which case we would expect  $\alpha < \alpha_{\text{eff}} < 1$ .
- In (4) we have introduced an additional parameter  $\zeta_j$  that adds the flexibility for the amplitude of the structure at a particular wavenumber index  $j$  to be modified from that predicted by the power law. This is because in practice we find the amplitude of the first component of the power law to be significantly less than that predicted by the power law. The fractional reduction is described by the parameter  $\zeta_1$ , while for all other wavenumbers no reduction is required (i.e.  $\zeta_j = 1$  for  $j > 1$ ).

The five parameters affect scattering behaviour in different ways, and their relative importance changes depending on the size of the particle relative to the wavelength, i.e. the value of  $x$ . For particles of a similar size to the wavelength, non-Rayleigh effects are governed by destructive interference between scattering from one side of the particle and the other. This is determined by the concentration of mass in the centre of the particle, which is affected in equal measure by the  $\alpha_{\text{eff}}$  and  $\kappa$  parameters. For much larger particles, the degree of scattering is dominated by the amount of structure within the particle at a scale similar to the wavelength. This is proportional to the energy in the power spectrum over a range of wavenumbers centred at  $j \simeq x/\pi$ . The power spectrum is described by  $\beta$  and  $\gamma$ , so both are important for large-particle scattering. The final term,  $\zeta_1$ , only affects one point in the power spectrum that is only really important for intermediate sizes.

### 2.3. Representing non-spherical monomers

If we use the Clausius–Mossotti value of  $K$  in (1), then in the limit of a small particle compared to the wavelength (i.e. when the ‘aggregate’ is reduced to just a single monomer crystal), the backscatter cross-section will be the same as that predicted by Rayleigh theory. However, Rayleigh theory is applicable only for spheres, so this is implicitly making the assumption that the monomer crystals are spherical, which of course they are not. The extension of Rayleigh theory to non-spherical particles that are nonetheless much smaller than the wavelength is commonly attributed to Gans and leads to a different value of  $K$  depending on the shape and orientation of the particle. We make the assumption that, if an isolated ice crystal scatters according to Gans theory with a particular value of  $K$ , then a larger aggregate composed of a

number of ice crystals of the same shape will scatter according to Rayleigh–Gans theory with the same value of  $K$ . This assumption is tested in section 4.

Gans theory describes the polarizability of a particle such that the effective dielectric factor along a primary axis  $x$  of the particle may be written as

$$K_x = \frac{(\epsilon - 1)/3}{1 + (\epsilon - 1)L_x}, \quad (5)$$

and similarly for the other axes  $y$  and  $z$ , where  $L_x$ ,  $L_y$  and  $L_z$  are geometric factors characterizing the shape of the particle. For a sphere,  $L = 1/3$  for all axes and it can be seen that  $K_x$  returns to the Clausius–Mossotti value in (2). Equations for the  $L$  terms were provided by van de Hulst (1957) for oblate and prolate spheroids as a function of their aspect ratio, and more recently Westbrook (2014) provided equations for hexagonal columns and plates:

$$\left. \begin{aligned} L_x = L_y &= \frac{1}{4} \left( \frac{1 - 0.5\alpha^{-0.9}}{1 + 0.5\alpha^{-0.9}} + 1 \right), \\ L_z &= \frac{1}{2} \left( \frac{1 - 3\alpha}{1 + 3\alpha} + 1 \right), \end{aligned} \right\} \quad (6)$$

where  $\alpha$  is the aspect ratio using the convention that numbers greater than 1 correspond to columns (note that this is the opposite convention to that used by Westbrook, 2014). Here,  $z$  is the axis of rotational symmetry in the case of spheroids and the axis of sixfold rotational symmetry in the case of hexagonal columns and plates. The geometric factors are the same in the  $x$  and  $y$  directions, and so  $L_x = L_y$  and  $K_x = K_y$ .

Gans theory has been applied in radar meteorology to compute the backscatter cross-section to horizontally and vertically polarized radiation of horizontally aligned oblate raindrops (Seliga and Bringi, 1976) and ice particles (Westbrook, 2014). In the present article we consider the individual monomer crystals within the aggregate to be randomly oriented. Therefore each axis contributes equally to the average dielectric factor of non-spherical particles,  $K_{\text{NS}}$ , defined as:

$$K_{\text{NS}}^2 = \frac{1}{3} (K_x^2 + K_y^2 + K_z^2) = \frac{2}{3} K_x^2 + \frac{1}{3} K_z^2. \quad (7)$$

The backscatter cross-section (1) and scattering cross-section are each proportional to  $|K_{\text{NS}}|^2$ , so we may define a non-spherical scattering enhancement factor  $|K_{\text{NS}}|^2/|K_{\text{CM}}|^2$ , where  $K_{\text{CM}}$  is the Clausius–Mossotti value for spheres. This is plotted in Figure 1(a) for 94 GHz, where it can be seen that randomly oriented non-spherical particles scatter systematically more than spheres of the same volume. This is because the increase in polarizability along the longest axes of non-spherical particles is larger than the decrease in polarizability along their shortest axes, leading to a net increase in the induced dipole moment, and hence in the intensity of the scattered radiation.

The dielectric factor  $K$  appears in a different way in the case of absorption cross-section, which in the Rayleigh approximation (e.g. van de Hulst, 1957) may be rewritten in terms of particle volume as

$$\sigma_a = 3kV \text{Im}(-K), \quad (8)$$

where  $\text{Im}$  denotes the imaginary part. Since in the RGA the electric field at any point in the particle is approximated by the incident field, the absorption cross-section is the same as predicted by Rayleigh theory, although with the modified value of  $K$ . Thus we are also concerned with the value of  $\text{Im}(-K)$ , noting that this is a positive number in the convention that the imaginary part of  $\epsilon$  is negative. Figure 1(b) depicts the non-spherical absorption enhancement  $\text{Im}(-K_{\text{NS}})/\text{Im}(-K_{\text{CM}})$ , which is again larger for non-spherical particles than for spheres.

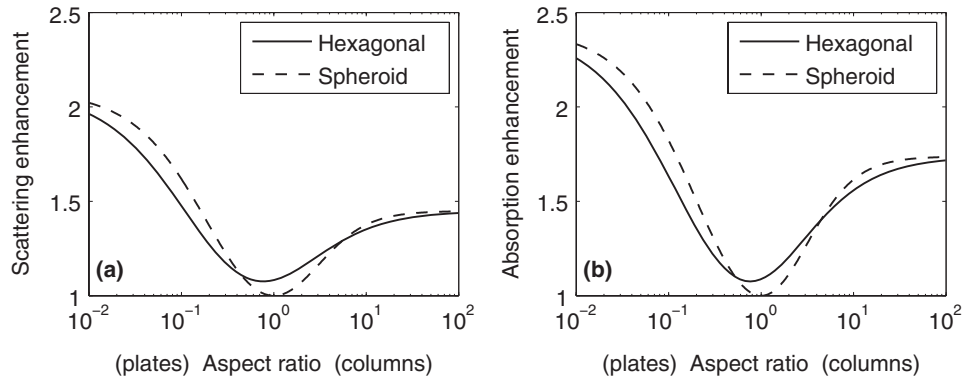


**Figure 1.** (a) Scattering enhancement factor due to the non-sphericity of monomers, versus aspect ratio, where the monomers are assumed to be randomly oriented within the aggregate. This factor is equal to  $|K_{NS}|^2/|K_{CM}|^2$ , where  $K_{NS}$  is as computed in section 2.3 and  $K_{CM}$  is the equivalent Clausius–Mossotti value. (b) The corresponding absorption enhancement factor, equal to  $\text{Im}(-K_{NS})/\text{Im}(-K_{CM})$ . The solid lines were computed from the geometric factors appropriate for hexagonal plates and columns, while the dashed lines were computed from geometric factors appropriate for oblate and prolate spheroids. Note that these functions are virtually identical at all microwave frequencies.

The improvements to scattering and absorption via the use of  $K_{NS}$  are verified against DDA calculations in section 4.2. Gans theory has been adapted only to simple shapes such as columns and plates, whereas the comparisons later in the article use bullet-rosette monomers. We find that the enhancements from assuming a hexagonal columnar monomer with an aspect ratio of 4 matches closely the DDA simulations of low-density aggregates composed of bullet-rosette monomers. Specifically, this aspect ratio predicts a scattering enhancement of 25% and an absorption enhancement of 38% at all microwave frequencies.

#### 2.4. The scattering phase function and scattering cross-section

We wish to extend the SSRGA to compute all scattering properties including the full scattering phase function, neglecting polarization in the first instance. This is achieved by extending (1) to all directions, recognizing that the scattering amplitude in any direction is determined by the degree of destructive interference from all the different parts of the particle. In the case of homogeneous spheres, this may be calculated from geometry following van de Hulst (1957): in the backscatter direction (scattering at an angle  $\theta$  of  $180^\circ$ ), the maximum difference in path length between two light rays each being scattered just once is  $2D$ . For scattering in an arbitrary direction, the maximum difference in path length is reduced to  $2D \sin(\theta/2)$ . In the forward direction there is no difference in path length and only constructive interference, leading to a preference for forward scattering. Thus, we may compute the scattering in any direction by using the same function  $\phi(x)$  but scaling its argument by  $\sin(\theta/2)$ ; therefore the equivalent of (1) for scattering angle  $\theta$  is

$$\sigma_s(\theta) = \frac{9}{4\pi} k^4 |K|^2 V^2 \phi \{x \sin(\theta/2)\} \frac{1 + \cos^2 \theta}{2}. \quad (9)$$

Here,  $\sigma_s(\theta)$  is defined as geometric cross-sectional area of an idealized particle that scatters all radiation incident upon it isotropically, and scatters the same amount of energy by angle  $\theta$  as the actual particle. Since each volume element acts as a Rayleigh scatterer, we have introduced the Rayleigh ‘dumb-bell’ scattering pattern via the  $(1 + \cos^2 \theta)/2$  term.

If we can compute the scattering in any direction then the scattering cross-section is found by integrating over all angles:

$$\sigma_s = \frac{1}{2} \int_0^\pi \sigma_s(\theta) \sin \theta \, d\theta. \quad (10)$$

Lord Rayleigh solved this analytically for spheres, although his solution contained the cosine integral so would be as easy nowadays to integrate numerically.

#### 2.5. Polarization considerations

Since the RGA treats a particle as a collection of non-interacting Rayleigh scatterers, it predicts the same very simple polarization properties as Rayleigh theory. In the backscatter direction, relevant for radar remote sensing, it predicts zero depolarization. This is a reasonable first-order approximation: Matrosov *et al.* (1996) observed the radar depolarization ratio of ice aggregates to be only around 5%. It also predicts that the radar backscatter of horizontally oriented particles viewed from the side should not depend on the axis of polarization of the transmitted wave. Hogan *et al.* (2012) reported observations of ice aggregates for which the 3 GHz radar backscatter was around 10% (0.5 dB) greater for horizontally than vertically polarized radiation. This suggests that we should not expect RGA backscatter calculations for ice aggregates to have an uncertainty of less than 10%.

At scattering angles other than  $180^\circ$ , we can adapt the predictions of Rayleigh theory to RGA. If the Plane of Scattering is defined as the plane containing the directions of propagation of both the incident and scattered radiation, then we may consider the incident radiation to be composed of a component polarized perpendicular to the plane (with intensity  $I_\perp$ ) and another polarized parallel to it (with intensity  $I_\parallel$ ), and consider the scattering of these components separately. Thus, the scattering of  $I_\perp$  will be completely polarized in exactly the same direction, with a scattered intensity governed by a modified version of (9) of the form

$$\sigma_\perp(\theta) = \frac{9}{4\pi} k^4 |K|^2 V^2 \phi \{x \sin(\theta/2)\}. \quad (11)$$

Likewise, the scattering of  $I_\parallel$  is also completely polarized and the direction of polarization of the scattered radiation is also parallel to the Plane of Scattering, but this time the scattered intensity is governed by

$$\sigma_\parallel(\theta) = \frac{9}{4\pi} k^4 |K|^2 V^2 \phi \{x \sin(\theta/2)\} \cos^2 \theta. \quad (12)$$

The polarization state of the scattered radiation can therefore be found from the relative magnitudes of  $I_\parallel$  and  $I_\perp$ . For unpolarized incident radiation ( $I_\parallel = I_\perp$ ) the total scattering is found by averaging (11) and (12), which correctly yields (9). But even for unpolarized incident radiation, the scattered radiation can be polarized, and as with Rayleigh scattering, the radiation scattered at an angle of  $\theta = 90^\circ$  is completely polarized because  $\sigma_\perp(90^\circ) = 0$ . Note that the evaluation of the SSRGA model in the remainder of this article considers only unpolarized radiation.

### 3. Fitting SSRGA parameters to synthetic aggregates

In this section, the five dimensionless parameters used by SSRGA to describe the structure of ice particles are estimated. The

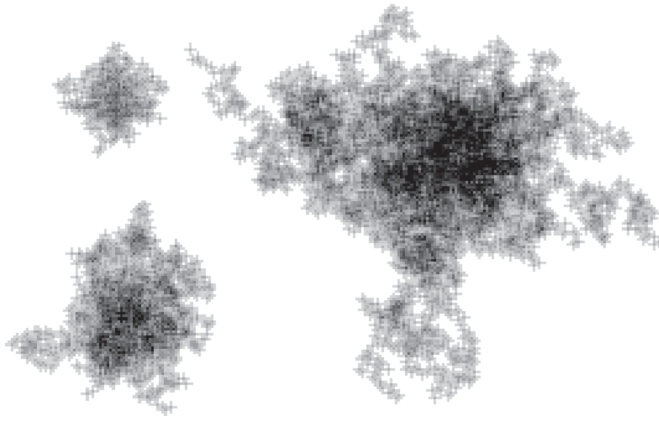


**Figure 2.** Two-dimensional images of aggregates generated by the Nowell *et al.* (2013) model with maximum dimensions of close to 2, 4 and 8 mm. The monomers were bullet rosettes with maximum dimension 200  $\mu\text{m}$ . The shading indicates the amount of ice in the third dimension.

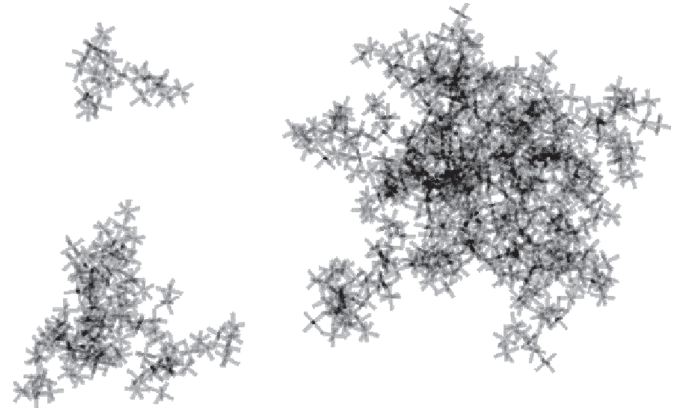


**Figure 3.** As Figure 2, but for aggregates generated by the Westbrook *et al.* (2004) model with maximum dimensions of close to 2, 4 and 8 mm. The monomers were bullet rosettes with maximum dimension 400  $\mu\text{m}$ .

SSRGA computes scattering parameters that are an average over an ensemble of particles of the same size. Therefore, to evaluate the scattering phase function we use two aggregate models to simulate a number of 3D aggregates of around the same size. We characterize the ice particles according to their maximum dimension  $D_{\text{max}}$ , the maximum distance between any two dipoles in the lattice. This article is primarily concerned with the scattering cross-section and scattering phase function in contexts where many scattering events may have taken place, and so the radiation incident on a particle is from a random direction with respect to the particle orientation. Therefore, we treat the particles as randomly oriented. Note that the backscatter cross-section of horizontally oriented particles can still be computed for a specific radar viewing angle by ensuring that for backscatter only, the  $\alpha_{\text{eff}}$  value used is the ratio of the particle size in the direction of propagation to the maximum dimension (Hogan *et al.*, 2012).

### 3.1. Synthetic aggregate models

Two aggregate models are used to generate synthetic particles. The first was devised by Nowell *et al.* (2013) and uses bullet-rosette monomer crystals of either 200 or 400  $\mu\text{m}$  in size. In this model the particle is described on a Cartesian lattice with each cell of the lattice being either completely full of ice or completely empty. Individual monomers are added one by one to an existing aggregate, and their placement is random, but with the constraint that a new monomer must touch but not overlap the existing ice in the lattice. The second model was devised by Westbrook *et al.* (2004) and attempts to simulate the process of aggregation physically. A population of particles is simulated simultaneously, each particle initially being a bullet-rosette monomer 400  $\mu\text{m}$  in size (in the implementation used in this article). Pairs of particles collide and stick at the first point of contact. This process is repeated, with the orientation of the particles being randomized between each collision. For further details about the models, the reader is referred to these two articles.

Example particle images from the Nowell *et al.* (2013) model using 200  $\mu\text{m}$  monomers are shown in Figure 2, and from the Westbrook *et al.* (2004) model in Figure 3. The two models produce particles with a rather different character: the Nowell *et al.* (2013) aggregates tend to have a dense core, while the Westbrook *et al.* (2004) aggregates have a more open structure. Of most relevance for microwave scattering is the mass of a particle, and specifically for this article, the applicability of the RGA relies on the particle density being quite low. Figure 4 depicts the volume fraction for particles generated by the two models as a function of size, i.e. the volume of ice in the particle,  $V$ , divided by the volume of a sphere of diameter  $D_{\text{max}}$ . For reference, three empirical relationships are shown. The first two were derived from aircraft observations of size distributions dominated by

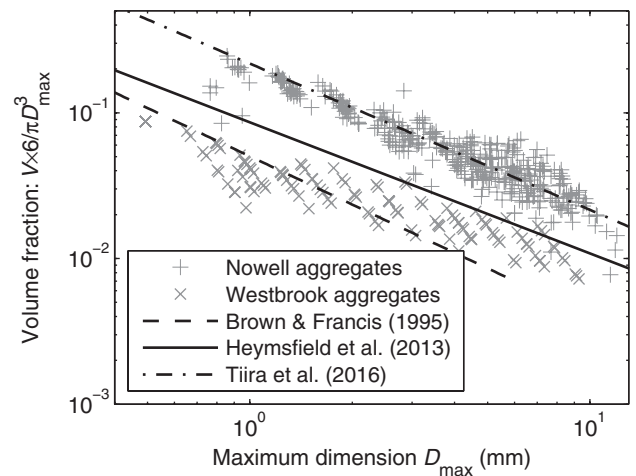


**Figure 4.** The volume fraction of aggregates generated by the Nowell *et al.* (2013) model (using bullet-rosette monomers of either 200 or 400  $\mu\text{m}$  in size) and the Westbrook *et al.* (2004) model (using bullet-rosette monomers of 400  $\mu\text{m}$  in size), as a function of maximum dimension, where  $V$  is the volume of ice in the particle. The volume fractions for three mass–size relationships are also plotted and are described in the text. The Brown and Francis (1995) relationship is not shown for  $D_{\text{max}} > 6$  mm, which is outside the range for which this relationship has been verified.

unrimed ice aggregates: the relationship of Brown and Francis (1995), when expressed in SI units in terms of  $D_{\text{max}}$  (Hogan *et al.*, 2012), has the form

$$m = 0.0121D_{\text{max}}^{1.9}, \quad (13)$$

where  $m$  is the particle mass. It was found by Hogan *et al.* (2006) and Hogan *et al.* (2012) that this relationship provided an excellent fit between *in situ* aircraft estimates and simultaneous radar observations of three different radar variables in the Rayleigh-scattering regime, for stratiform clouds at temperatures between  $-10$  and  $-47^\circ\text{C}$ . The second relationship is from Heymsfield *et al.* (2013), who used a large, state-of-the-art aircraft database at temperatures between  $0$  and  $-86^\circ\text{C}$  to fit the following (in SI units):

$$m = 0.0824D_{\text{max}}^{2.1}. \quad (14)$$

Simultaneous observations of size distributions and snow accumulation at the surface tend to show snowflakes to be denser than those observed by aircraft, presumably due to the higher occurrence of riming near the surface. For example, Tiira *et al.* (2016) found that a large database of snow observations at a surface site in Finland were consistent with the following relationship (SI units):

$$m = 0.102D_{\text{max}}^{1.996}. \quad (15)$$

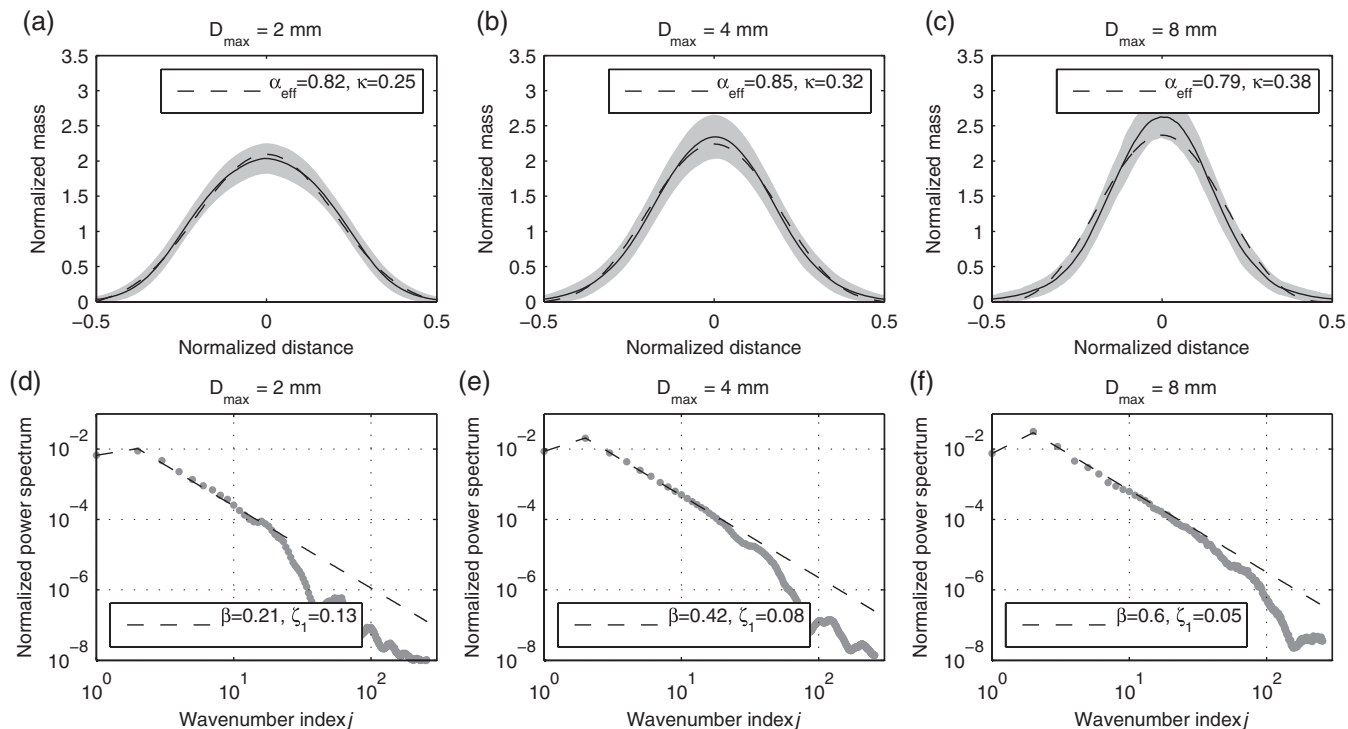


**Figure 5.** Illustration of the extraction of the parameters describing the structure of aggregates needed by the SSRGA, using randomly oriented aggregates generated by the Nowell *et al.* (2013) model from 200  $\mu\text{m}$  monomers. Panels (a)–(c) characterize the mean shape of particles with maximum dimension of 2, 4 and 8 mm. The black solid line shows the mean normalized  $A(s)$  function of the simulated aggregates, with the shaded region indicating one standard deviation. The dashed line fits this with the  $A_{\text{fit}}(s)$  function given by (16). Panels (d)–(f) characterize the internal structure of the same particles. The grey dots indicate power spectra of the internal structure, i.e. of deviations from the fit in real aggregates. The dashed line indicates that at lower wavenumbers corresponding to structure larger than individual monomers, this may be fitted by a power law proportional to  $\beta(2j)^{-\gamma}$ , where  $\gamma = 7/3$  for these particles.

In Figure 4 it can be seen that the Westbrook *et al.* (2004) aggregates typically lie between the two aircraft-derived curves, while the Nowell *et al.* (2013) aggregates are significantly denser and are consistent with rimed snowflakes observed at the surface. Thus the two aggregate models provide an opportunity to test the validity of the RGA (on which the SSRGA relies) both for unrimed particles, and for particles with a density typical of snowflakes which have experienced some degree of riming.

Even if their mass–size relationships are realistic, the morphology of synthetic aggregates is an imperfect representation of reality, which may limit the applicability of the results somewhat. Observations of aggregates in cirrus clouds colder than  $-25^\circ\text{C}$  find that aggregates composed of up to around ten bullet-rosette monomers are common (Heymsfield *et al.*, 2002; Um and McFarquhar, 2007); their appearance in airborne probe imagery is very similar to the Westbrook *et al.* (2004) aggregates up to 2 mm in size (e.g. the smallest image in Figure 3). For larger particles, intended to represent snowflakes at higher temperatures, we simply considered aggregates composed of more monomers of the same size, rather than increasing the monomer size. This is partially justified by the finding of Hogan and Westbrook (2014) that the SSRGA is insensitive to the shape of the monomer particles, provided that they are considerably smaller than the wavelength of the radiation. High-resolution imagery of free-falling snow aggregates at the surface show them to be commonly composed of dendrites (e.g. Garrett and Yuter, 2014), crystals that themselves have structures at much smaller scales. Therefore, the synthetic aggregates used in this article should be sufficient to test the validity of SSRGA for large particles, but there remains a need for future work to derive the five SSRGA parameters for alternative 3D models of snow aggregates.

### 3.2. Fitting SSRGA parameters

The five properties needed by the SSRGA were described in section 2.2. The process to estimate them is similar to that described by Hogan and Westbrook (2014). Suppose that we

have  $n$  3D aggregates of a particular size. To reduce statistical uncertainty, we reorient each particle randomly 50 times, and sample each reoriented particle along its three orthogonal directions, yielding a total of  $150n$  samples. For each sample, a 1D function  $A(s)$  is generated consisting of the total area of ice intersected by a plane at distance  $s$ . The maximum extent of the particle along this dimension is  $D$  used in the SSRGA. Since particles are usually characterized by their maximum dimension  $D_{\text{max}}$ , we compute the first property, the effective aspect ratio:  $\alpha_{\text{eff}} = \overline{D}/D_{\text{max}}$ , where the average is taken over the  $150n$  samples.

The second property characterizes the extent to which the mass is concentrated toward the centre of the particle. This is done by normalizing the  $A(s)$  function in two ways: the dimension  $s$  is divided by  $\overline{D}$  so that the average particle extent in this dimension is unity, and it is offset in  $s$  so that the ‘centre of gravity’ is at  $s = 0$ . It is then normalized so that the integral of  $A$  in this range is 1, and the  $150n$  normalized functions are averaged in the range  $-0.5$  to  $+0.5$ . This results in the solid black lines in Figures 5(a)–(c) for Nowell *et al.* (2013) aggregates composed of 200  $\mu\text{m}$  bullet rosettes, and the same in Figures 6(a)–(c) for Westbrook *et al.* (2004) aggregates. The grey region indicates the one-standard-deviation variability of individual samples from the mean. The mean shape is then fitted by the function

$$A_{\text{fit}}(s) = \frac{\pi}{2} \left\{ \left( 1 + \frac{\kappa}{3} \right) \cos(\pi s) + \kappa \cos(3\pi s) \right\}, \quad (16)$$

where the kurtosis parameter  $\kappa$  is chosen to give the same variance as the actual mean function. It can be seen that (16) provides a reasonably good fit to the mean shape, and  $\kappa$  quantifies something that can be seen visually in Figures 2 and 3: as the Nowell *et al.* (2013) particles get larger they tend to concentrate more mass in the centre with increasingly tenuous extremities, while the Westbrook *et al.* (2004) particles are more self-similar; their structural parameters vary less with size.

Next we characterize the internal structure of the particle. The functional fit  $A_{\text{fit}}(s)$  is subtracted from each individual  $A(s)$  function to yield purely the deviation from the mean shape.

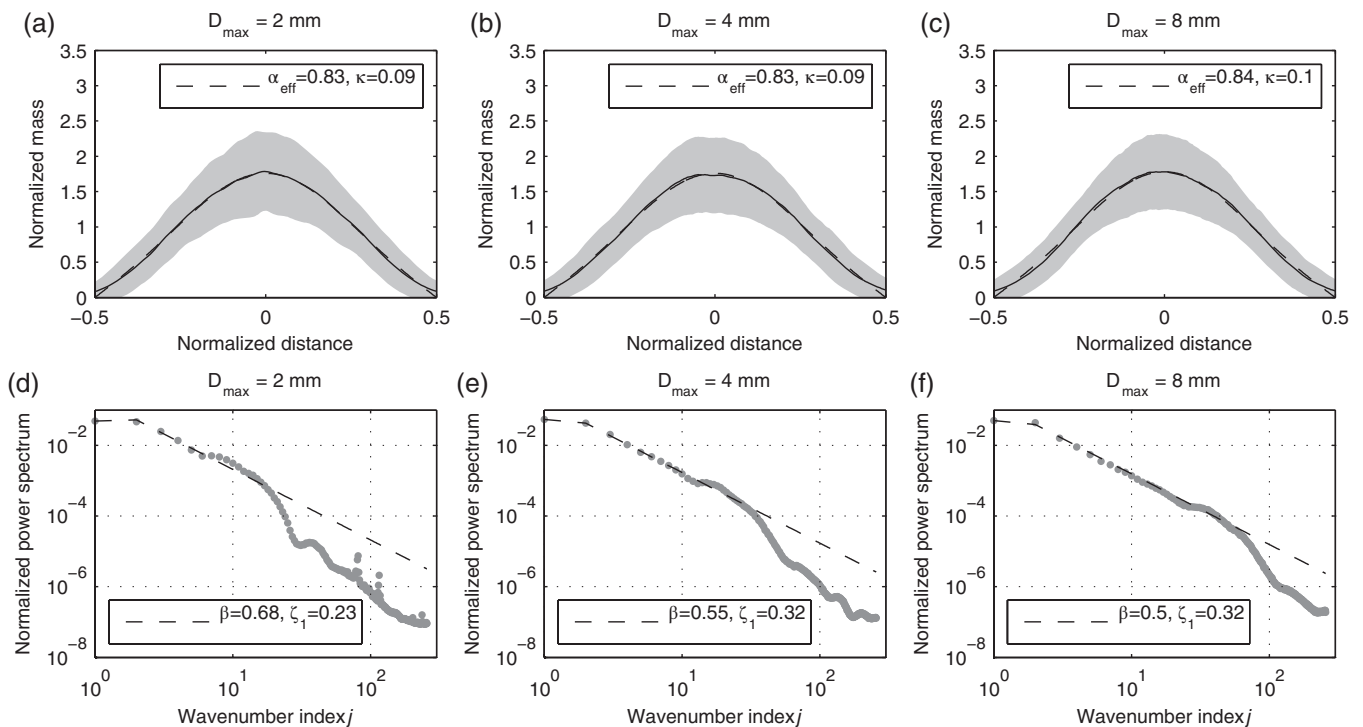


Figure 6. As Figure 5, but for aggregates generated by the Westbrook *et al.* (2004) model, and fitting the power spectra by power laws with  $\gamma = 2$ .

Power spectra are then computed for each sample in the range  $-0.5 < s < 0.5$ , and averaged in wavenumber space. The results are shown in Figures 5(d)–(f) and 6(d)–(f). The low wavenumber structure, corresponding to scales larger than that of individual monomers, exhibit self-similar behaviour since the spectra are well fitted by power laws shown by the dashed lines. The slope of the power law is close to  $\gamma = 7/3$  for the Nowell *et al.* (2013) aggregates and  $\gamma = 2$  for the Westbrook *et al.* (2004) aggregates. The difference is likely to be because the Westbrook *et al.* (2004) model allows one aggregate to join onto another, maintaining more structure at all scales, whereas the Nowell *et al.* (2013) model only allows an aggregate to grow by accreting single crystals, leading to a more ‘foam-like’ structure. Note that a slope of  $\gamma = 2$  is steeper than the  $5/3$  found by Hogan and Westbrook (2014) for the Westbrook *et al.* (2004) aggregate model, but their fitting procedure was slightly different and only particles of one size were analyzed. The steeper power spectrum at high wavenumbers corresponds to monomer scales, but these do not affect the scattering properties significantly provided that the wavelength of the radiation is larger than the smallest scales present in the particle.

Finally, the  $\beta$  and  $\zeta_1$  parameters are estimated. It can be seen from the figures that the first element of the power spectrum ( $j = 1$ ) is systematically lower than the value that would be found by fitting a power law, so this point is treated separately. The parameter  $\beta$  is therefore fitted to the power spectrum from  $j = 2$  to 12, this upper limit being chosen to ensure we do not sample the steepening of the slope at monomer scales. By Parseval’s theorem, the integral of the power spectrum equals the variance of the field from which it was calculated,  $A(s) - A_{\text{fit}}(s)$  and, moreover, a particular element of the power spectrum is equal to the contribution of a specific wavenumber to the total variance. From the way the fitted spectrum is constructed (described by Hogan and Westbrook, 2014), it can be shown that the variance due to wavenumber  $j$  of the fitted spectrum is equal to  $(\pi^2/8)\beta(2j)^{-\gamma}$ . Therefore,  $\beta$  may be computed such that the sum of the fitted spectrum for  $2 \leq j \leq 12$  equals the actual power spectrum over this range of wavenumbers. The parameter  $\zeta_1$  is then simply the ratio of the actual and fitted power spectrum at  $j = 1$ . The fitted parameters are shown in the legends of Figures 5 and 6.

To ensure a smooth variation of SSRGA scattering properties across the range of particle sizes of interest (1–10 mm), we have

Table 1. Fits for the five parameters.

Parameter	Nowell <i>et al.</i>	Westbrook <i>et al.</i>
$\alpha_{\text{eff}}$	0.82	0.83
$\kappa$	$0.16D_{\text{max}}^{0.44}$	0.09
$\beta$	$0.15D_{\text{max}}^{0.64}$	$0.86D_{\text{max}}^{-0.3}$
$\gamma$	7/3	2
$\zeta_1$	$0.22D_{\text{max}}^{-0.44}$	0.28

$D_{\text{max}}$  is in millimetres and the range of validity of the fits is limited to 1–10 mm.

fitted expressions for the five parameters to the values found for the discrete sizes shown in Figures 5 and 6. When there is insufficient variation of a parameter to justify a size dependence, a constant value is used. In the case of the Nowell *et al.* (2013) model, we also include particles of size  $D_{\text{max}} = 1$  mm in the fit, and average the results for aggregates of 200  $\mu\text{m}$  monomers and aggregates of 400  $\mu\text{m}$  monomers. For each discrete size, there are typically ten different particles, each sampled from 150 different angles. The fits for the Nowell *et al.* (2013) and the Westbrook *et al.* (2004) aggregate models are shown in Table 1.

#### 4. Evaluation against DDA calculations

Scattering calculations have been performed using the DDA for particles generated by the two aggregate models. Scattering by the Nowell *et al.* (2013) aggregates used the ‘DDSCAT’ model of Draine and Flatau (1994), while scattering by the Westbrook *et al.* (2004) aggregates used the ‘A-DDA’ model of Yurkin and Hoekstra (2011). Calculations were performed at 94 GHz using an ice refractive index of  $1.78306 - 0.0019734i$ , and at 183.31 GHz using a refractive index of  $1.78306 - 0.003862i$ . In section 4.1 we evaluate the phase functions predicted by SSRGA for particles of specific sizes, and in section 4.2 comparisons over a wider range of particle size are performed to evaluate scattering and absorption cross-sections, and the asymmetry factor.

##### 4.1. Evaluation of the scattering phase function

We first test the ability of SSRGA to predict the scattering phase function,  $p$ , which specifically tests the angular distribution

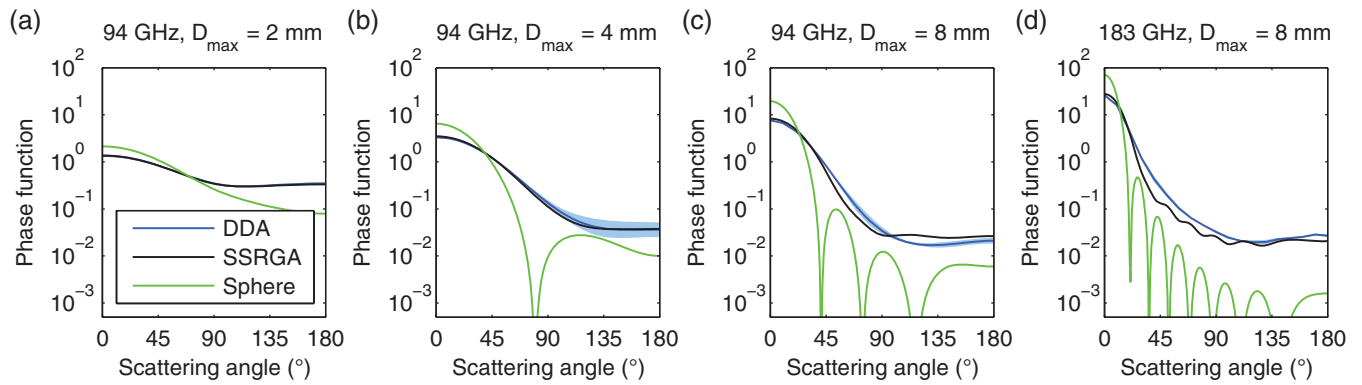


**Figure 7.** Comparison of the phase functions of ensembles of aggregates of 200  $\mu\text{m}$  bullet rosettes, generated using the Nowell *et al.* (2013) model, for the frequencies and maximum dimensions ( $D_{\text{max}}$ ) indicated above each panel. The blue lines and blue shaded regions show the mean and standard deviation of DDA calculations, while the black lines show the SSRGA calculations using the fitted parameters shown in Figure 5. The green lines show the equivalent phase functions for soft spheres with the same mass and with a diameter of  $\alpha_{\text{eff}}D_{\text{max}}$ . The RMS fractional differences between the SSRGA and DDA phase functions for each panel are: (a) 0.02, (b) 0.09, (c) 0.31, and (d) 0.33.

resulting from (9). We use the definition  $p(\theta) = \sigma_s(\theta)/2\sigma_s$ , where  $\sigma_s$  is the scattering coefficient given by (10). This normalization ensures that  $\int_0^\infty p(\theta) \sin(\theta) d\theta = 1$ , and makes  $p$  insensitive to parameters that scale the overall scattering of the particle, such as the volume of ice  $V$  or the dielectric factor  $K$ .

Figures 7(a)–(c) depict the 94 GHz phase functions for the three particle sizes of the Nowell *et al.* (2013) model shown in Figure 5, and Figure 7(d) shows 183 GHz calculations for 8 mm particles. Figure 8 shows the same but for the Westbrook *et al.* (2004) aggregate model. The DDA calculations have been averaged over all orientations and over the ensemble of particles available at each size. The shaded regions show the one-standard-deviation spread in DDA calculations from the different particles of the same size. Since SSRGA is intended to provide an ensemble average over many particles of the same size, only a single line is provided in each case.

The agreement between the shape of the DDA phase function ( $p_{\text{DDA}}$ ) and the SSRGA phase function ( $p_{\text{SSRGA}}$ ) is good for both the aggregate models, particularly in the forward and backward directions. To quantify the error in  $p_{\text{SSRGA}}$ , the RMS fractional difference with  $p_{\text{DDA}}$  has been computed as the root-mean-square of  $\ln(p_{\text{SSRGA}}/p_{\text{DDA}})$ . The values are presented in the captions of Figures 7 and 8. The largest error of 33% is for 8 mm Nowell *et al.* (2013) aggregates observed at 183 GHz, although this is far smaller than the three order-of-magnitude range spanned by the phase function. Moreover, all errors are much less than the RMS differences between the DDA calculations for Nowell *et al.* (2013) and Westbrook *et al.* (2004) aggregates of the same size at the same wavelength (presented in the caption of Figure 8). This gives us confidence that (9) provides a good approximation to the phase function for ice aggregates, with a typical error that is less than the uncertainty due to not knowing the exact ice particle shape.

The phase functions for equivalent ‘soft spheres’ consisting of a homogeneous ice–air mixture are very different from the DDA and SSRGA results, showing far too strong a preference for forward scattering. Note that we have used spheres with diameter  $\alpha_{\text{eff}}D_{\text{max}}$ , the average extent of the particle over all directions. An alternative sometimes used in the literature is spheres with diameter  $D_{\text{max}}$ , but these give results even more different from DDA. Note that Rayleigh–Gans and Mie theory give virtually identical phase functions for spheres with the densities considered here.

#### 4.2. Evaluation of cross-sections and asymmetry factor

Figures 9 and 10 evaluate SSRGA calculations of the asymmetry factor and the various cross-sections against DDA calculations for a wider range of particle sizes. The SSRGA calculations used the exact volumes of the particles, and the parameters given by Table 1. In order to specifically isolate non-Rayleigh effects, the

strong dependence on ice volume ( $V$ ) has been factored out by normalizing the cross-sections by the appropriate power of  $V$ . Thus Rayleigh scattering would predict perfectly horizontal lines in all panels. Also shown by the green lines are the values for soft spheres.

We consider first the asymmetry factor  $g$ , which is computed from the phase functions. Since the SSRGA phase functions agreed well with DDA in Figures 7 and 8, SSRGA also predicts  $g$  accurately. At 94 GHz, Figure 9(d) shows that SSRGA matches the DDA result that the Nowell *et al.* (2013) aggregates have lower  $g$  than Westbrook *et al.* (2004) at smaller sizes and higher  $g$  at larger sizes. This can be explained as follows. The first deviation from Rayleigh scattering at small sizes is governed by the overall shape of the particle as described by the kurtosis parameter  $\kappa$ . Since the Nowell *et al.* (2013) aggregates have higher  $\kappa$ , indicating that their mass is more concentrated toward their centre, deviations from Rayleigh scattering are not significant until they reach larger overall sizes (as measured by  $D_{\text{max}}$ ). For much larger particles, the amount of scattering in the backward and sideways directions is governed by the amplitude of the structure at around the scale of the wavelength, as determined by the  $\beta$  and  $\gamma$  parameters of the power law fit. Since large Westbrook *et al.* (2004) aggregates have more small-scale structure (indicated particularly by the smaller value of  $\gamma$ ) than Nowell *et al.* (2013) aggregates, they have more back- and side-scattering, and hence a lower  $g$ .

Consider next the absorption cross-section,  $\sigma_a$ . Over all size ranges, soft spheres underestimate the absorption. This is due to the implicit assumption of spherical monomers, which scatter and absorb systematically less than randomly oriented non-spherical particles, as explained in section 2.3. Our SSRGA calculations use a dielectric factor  $K_{\text{NS}}$  calculated assuming the monomers to be columns of aspect ratio 4, leading to excellent agreement with DDA calculations for Westbrook *et al.* (2004) aggregates at 94 GHz. Since absorption in the RGA is proportional to the volume of ice (8), any deviation of  $\sigma_a/V$  from a constant in the figures must be due to deviations from RGA. The DDA calculations reveal that for the Nowell *et al.* (2013) aggregates,  $\sigma_a/V$  increases by around 25% between 1 and 10 mm, indicating that the density of the particles is too high for the RGA (and hence the SSRGA) to be strictly valid.

In the case of scattering and backscatter cross-sections, SSRGA provides an excellent fit to DDA for the Westbrook *et al.* (2004) aggregates at both 94 and 183.31 GHz. In Figure 9(c), SSRGA correctly predicts the ‘cross-over’ between the backscatter cross-section of the Nowell *et al.* (2013) and Westbrook *et al.* (2004) aggregates. This occurs for the same reason as the cross-over found for asymmetry factor and discussed above. Again due to the density of the Nowell *et al.* (2013) aggregates being too large for the RGA to be strictly valid, it tends to underestimate these quantities for this aggregate model. Nonetheless, it is still a much better approximation than soft spheres, which drastically

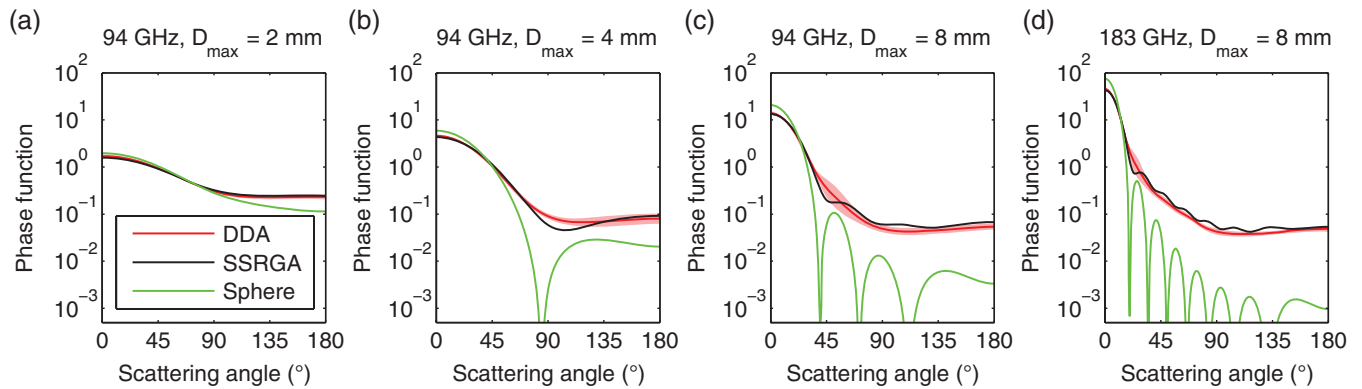


**Figure 8.** As Figure 7, but for aggregates generated by the Westbrook *et al.* (2004) model, with SSRGA parameters taken from Figure 6. The colours in this figure and Figure 7 are used to distinguish the aggregate types in the remaining figures of this article. The RMS fractional differences between the SSRGA and DDA phase functions for each panel are: (a) 0.06, (b) 0.20, (c) 0.24, and (d) 0.21. The RMS fractional differences between the DDA phase functions shown here and in the equivalent panels in Figure 7 are: (a) 0.25, (b) 0.48, (c) 0.72, and (d) 0.50.

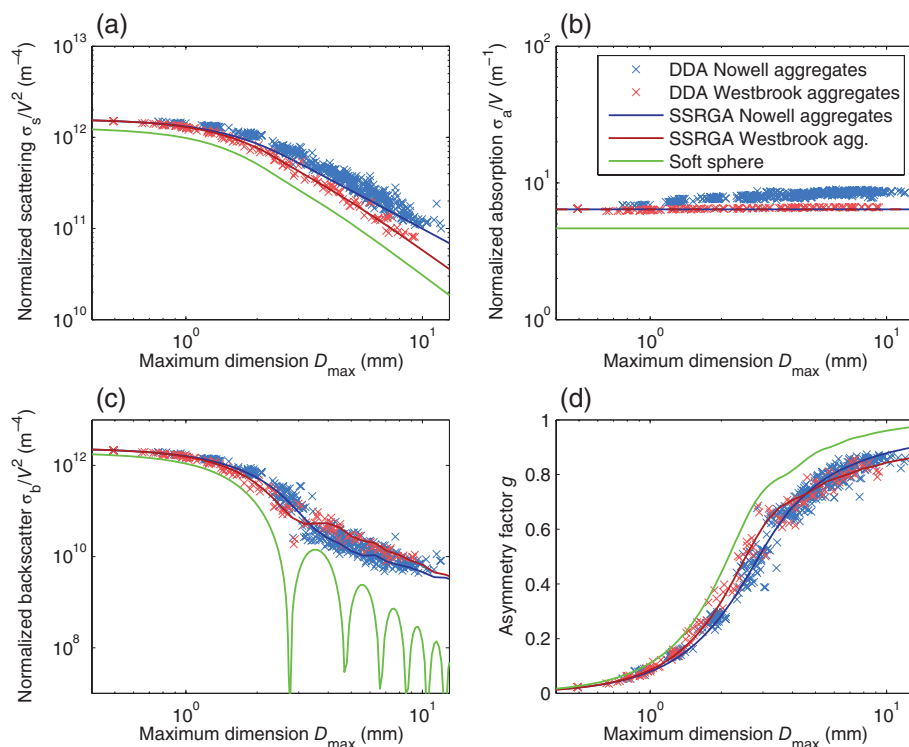


**Figure 9.** Comparison of the 94 GHz (a) scattering cross-section  $\sigma_s$ , (b) absorption cross-section  $\sigma_a$ , (c) backscatter cross-section  $\sigma_b$  and (d) asymmetry factor  $g$ , for individual aggregates generated by the Nowell *et al.* (2013) model (with monomers of either 200 or 400  $\mu\text{m}$  in size) and individual aggregates generated by the Westbrook *et al.* (2004) model. The SSRGA calculations used the exact volumes of the particles, and the parameters given by Table 1. The strong dependence on ice volume ( $V$ ) has been factored out by normalizing the scattering and backscatter cross-sections by  $V^2$  and the absorption cross-section by  $V$ . The green lines show the equivalent lines but for soft spheres with a diameter of  $\alpha_{\text{eff}} D_{\text{max}}$ .

underestimate both cross-sections to an increasing degree as the particles get larger.

To verify that the worse performance for the Nowell *et al.* (2013) aggregates is due to the RGA not being valid, rather than a weakness in the SSRGA equation or fitting procedure, we have gone back to original Rayleigh–Gans equation (e.g. Eq. (1) of Hogan and Westbrook, 2014) and explicitly computed the RGA backscatter cross-section from the full 3D structures of a range of particles from the two aggregate models considered in this article. As with DDA calculations, random orientation is assumed by averaging over many different orientations. It is still necessary to apply the non-spherical correction to the RGA described in section 2.3. The results are shown in Figure 11. It can be seen that in all cases SSRGA and RGA agree with each other within the uncertainty, verifying that any weakness in the SSRGA must be due to the underlying assumptions in the RGA being invalidated. We also see that for the Westbrook *et al.* (2004) aggregates, RGA and SSRGA are not significantly different from the equivalent DDA calculations at either frequency, whereas for the Nowell

*et al.* (2013) aggregates both underestimate the backscatter due to the particles being too dense for the RGA to be strictly valid.

Tyynelä *et al.* (2013) examined the validity of the RGA in detail for ice aggregates up to 220 GHz. In the case of backscatter coefficient, they reported underestimates of between 20 and 70%. The first point to note is that they applied the RGA using the Claussius–Mossotti value of  $K$ , implicitly assuming spherical monomers. Section 2.3 explains that much of this error can be explained by the enhancement due to non-spherical monomers. As an example, Tyynelä *et al.* (2013) reported that the backscatter by aggregates composed of thin hexagonal plates with an aspect ratio of 0.01 was underestimated by between 25 and 65%. Figure 1(a) shows that such plates have a spherical enhancement factor of 1.96, which if applied to their RGA calculations would remove the systematic underestimate and change the reported error to be between  $-30$  and  $+50\%$ . For some of the particle types considered by Tyynelä *et al.* (2013), the non-spherical monomer enhancement cannot explain all of the RGA underestimate. Indeed, some of their 8 mm particles had

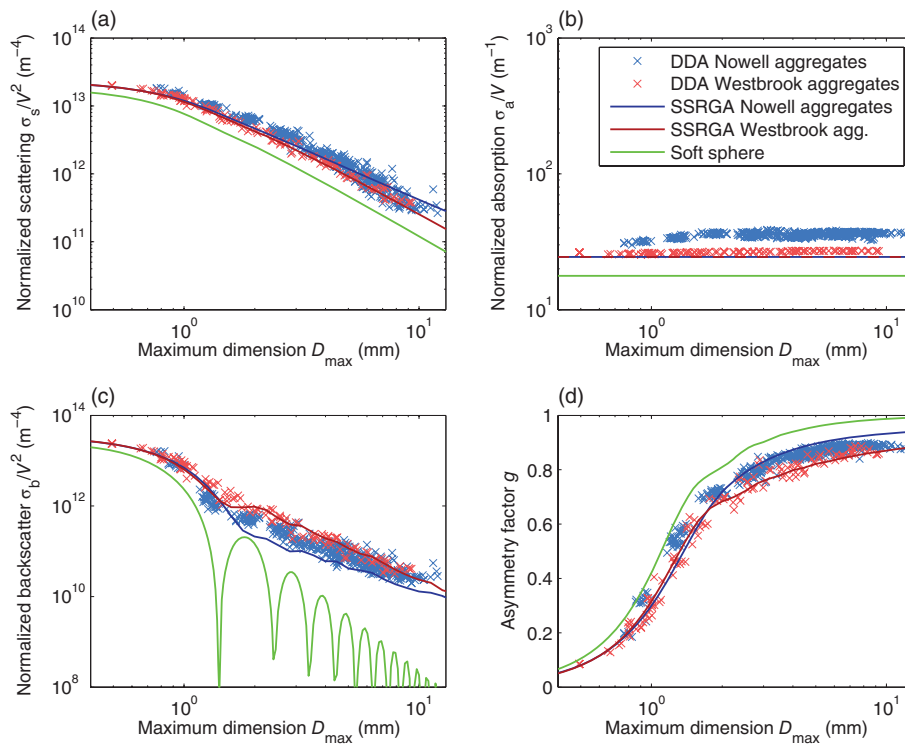


Figure 10. As Figure 9, but at 183.31 GHz.

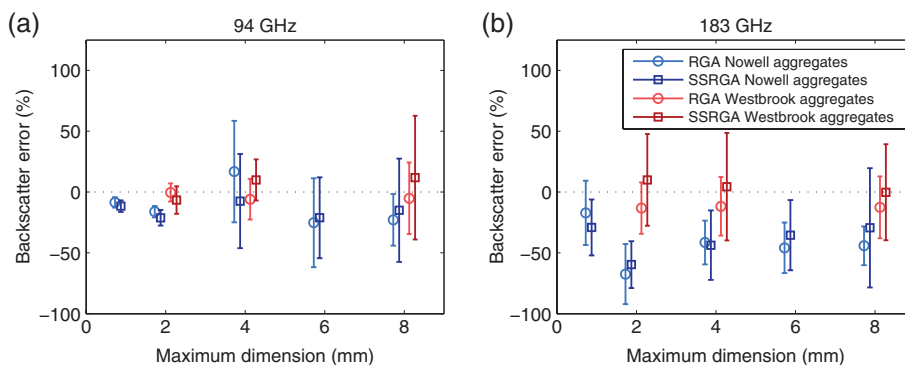


Figure 11. Error in backscatter cross-section computed by the Rayleigh–Gans Approximation (RGA) and the Self-Similar Rayleigh–Gans Approximation (SSRGA) for Nowell *et al.* (2013) and Westbrook *et al.* (2004) aggregates at (a) 94 GHz and (b) 183.31 GHz. ‘Backscatter error’ is defined simply as the difference with benchmark DDA calculations for the same particle. The error bars represent 95% of the range of the individual particles for each size. For clarity, the error bars have been offset horizontally from their reference values of maximum dimension of 1, 2, 4, 6 and 8 mm.

masses five times larger than predicted by the Heymsfield *et al.* (2013) relationship, which Figure 4 indicates are more similar to the density of the Nowell *et al.* (2013) aggregates considered in this article. For such particles, their finding of an underestimate of backscatter cross-section is consistent with our Figure 11.

Petty and Huang (2010) reported that the RGA underestimated backscatter coefficient by 2 dB for small particles and up to 7 dB for larger particles. They used monomers with extreme aspect ratios so, according to the results in section 2.3, a backscatter enhancement of around 2 dB should be applied at all sizes. This leaves a difference of up to 5 dB to be explained. Tyynelä *et al.* (2013) argued that this discrepancy was coincidental: Petty and Huang (2010) used only two sample aggregates, yet the RGA backscatter for individual particles can differ considerably from DDA at some sizes, even when averaged over orientation, and the bias of RGA is much smaller when averaging over many particles of the same size.

### 5. Conclusions

It is now widely recognized that homogeneous spheres and spheroids provide a poor approximation for computing the millimetre-wave scattering properties of snowflakes when the

particles are larger than the wavelength. Despite its accuracy, the current state-of-the-art, applying the Discrete Dipole Approximation (DDA) to a large number of individual simulated particles, is very computationally costly, and users of pre-generated DDA databases are stuck with the mass–size relationship of the particles used in generating the dataset.

Hogan and Westbrook (2014) introduced the Self-Similar Rayleigh–Gans Approximation (SSRGA) to compute the backscatter cross-section of unrimed ice aggregates at millimetre wavelengths. SSRGA is much faster and more convenient to use than DDA. This article extends the method to compute also the scattering and absorption cross-sections, as well as the full scattering phase function and parameters derived from it such as asymmetry factor. The error compared to benchmark DDA calculations is typically within the spread due to variations between different particles.

As part of this development, we have introduced a modification to the underlying RGA to account for an aggregate being composed of non-spherical, randomly oriented monomers, which scatter systematically more than spheres. This non-spherical enhancement explains previous findings (e.g. by Tyynelä *et al.*, 2013) that RGA underestimates backscatter even for particles of low enough density that the RGA ought to be applicable.

This brings into sharper focus the situations in which the RGA (and hence SSRGA) genuinely underestimates scattering, which appears to be limited to ice particles that are dense enough that they must have grown by riming in addition to aggregation. Even for rimed particles, the SSRGA is still much more accurate than soft spheres, and so could still be useful in that regime, perhaps after some tuning of the SSRGA parameters. Another interesting avenue would be to extend SSRGA to represent second-order scattering effects using an approach such as mean-field theory (Berry and Percival, 1986) or a more explicit method (e.g. Acquista, 1976; Lu *et al.*, 2014).

The SSRGA requires the structure of ice particles to be described by five parameters, which we have derived and parametrized for two different aggregate models. The aggregates generated by the two models are visually very different, and the five parameters provide a framework to explain quantitatively how the differences in structure lead to different scattering properties. For practical applications, the accuracy of SSRGA is limited by the realism of the synthetic aggregates from which the five parameters were derived. Large snow aggregates have a much more complex appearance than aggregates of bullet rosettes found in cirrus, so further work is required to generate more realistic 3D snowflake structures from which the SSRGA parameters can be derived, and to evaluate them using observations such as triple-frequency radar (e.g. Kneifel *et al.*, 2016).

The ability of SSRGA to predict the full range of unpolarized scattering properties is potentially useful for other particle regimes where the RGA is applicable, such as light scattering by aerosol aggregates (Sorensen, 2001). It is also worth noting that SSRGA scales easily to particles much larger than the wavelength for which the computational cost of DDA becomes prohibitive.

## Acknowledgements

We thank Alan Geer and Chris Westbrook for useful discussions. R. Honeyager acknowledges NASA grant NNX13AQ39G.

## References

Acquista C. 1976. Light scattering by tenuous particles: A generalization of the Rayleigh-Gans-Rocard approach. *Appl. Opt.* **15**: 2932–2936.

Battaglia A, Westbrook CD, Kneifel S, Kollias P, Humpage N, Löhnert U, Tyynelä J, Petty GW. 2014. G-band atmospheric radars: New frontiers in cloud physics. *Atmos. Meas. Tech.* **7**: 1527–1546.

Bauer P, Moreau E, Chevallier F, O’Keeffe U. 2006. Multiple-scattering microwave radiative transfer for data assimilation applications. *Q. J. R. Meteorol. Soc.* **132**: 1259–1281.

Berry MV, Percival IC. 1986. Optics of fractal clusters such as smoke. *Opt. Acta* **33**: 577–591.

Brown PRA, Francis PN. 1995. Improved measurements of the ice water content in cirrus using a total-water probe. *J. Atmos. Oceanic Technol.* **12**: 410–414.

Buehler SA, Jiménez C, Evans KF, Eriksson P, Rydberg B, Heymsfield AJ, Stubenrauch CJ, Lohmann U, Emde C, John VO, Sreerexha TR, Davis CP. 2007. A concept for a satellite mission to measure cloud ice water path, ice particle size, and cloud altitude. *Q. J. R. Meteorol. Soc.* **133**: 109–128.

Delanoë J, Hogan RJ, Forbes RM, Bodas-Salcedo A, Stein THM. 2011. Evaluation of ice cloud representation in the ECMWF and UK Met Office models using CloudSat and CALIPSO data. *Q. J. R. Meteorol. Soc.* **137**: 2064–2078.

Draine BT, Flatau PJ. 1994. Discrete-dipole approximation for scattering calculations. *J. Opt. Soc. Am. A* **11**: 1491–1499.

Garrett TJ, Yuter SE. 2014. Observed influence of riming, temperature, and turbulence on the fallspeed of solid precipitation. *Geophys. Res. Lett.* **41**: 6515–6522, doi: 10.1002/2014GL061016.

Geer AJ, Baordo F. 2014. Improved scattering radiative transfer for frozen hydrometeors at microwave frequencies. *Atmos. Meas. Tech.* **7**: 1839–1860.

Geer A, Baordo F, Bormann N, English SJ. 2014. *All-Sky Assimilation of Microwave Humidity Sounders*, Technical Memorandum 741. ECMWF: Reading, UK.

Heymsfield AJ, Lewis S, Bansemmer A, Iaquinta J, Miloshevich LM. 2002. A general approach for deriving the properties of cirrus and stratiform ice cloud particles. *J. Atmos. Sci.* **59**: 3–29.

Heymsfield AJ, Schmitt C, Bansemmer A. 2013. Ice cloud particle size distributions and pressure-dependent terminal velocities from in situ observations at temperatures from 0° to –86°. *J. Atmos. Sci.* **70**: 4123–4154.

Hogan RJ, Battaglia A. 2008. Fast lidar and radar multiple-scattering models – 2. Wide-angle scattering using the time-dependent two-stream approximation. *J. Atmos. Sci.* **65**: 3636–3651.

Hogan RJ, Illingworth AJ. 1999. The potential of spaceborne dual-wavelength radar to make global measurements of cirrus clouds. *J. Atmos. Oceanic Technol.* **16**: 518–531.

Hogan RJ, Westbrook CD. 2014. Equation for the microwave backscatter cross section of aggregate snowflakes using the self-similar Rayleigh–Gans approximation. *J. Atmos. Sci.* **71**: 3292–3301.

Hogan RJ, Mittermaier MP, Illingworth AJ. 2006. The retrieval of ice water content from radar reflectivity factor and temperature and its use in the evaluation of a mesoscale model. *J. Appl. Meteorol. Climatol.* **45**: 301–317.

Hogan RJ, Tian L, Brown PRA, Westbrook CD, Heymsfield AJ, Eastment JD. 2012. Radar scattering from ice aggregates using the horizontally aligned oblate spheroid approximation. *J. Appl. Meteorol. Climatol.* **51**: 655–671.

van de Hulst HD. 1957. *Light Scattering by Small Particles*. John Wiley and Sons: New York, NY. Reprinted 2003 by Dover Publications: Mineola, NY.

Illingworth AJ, Barker HW, Beljaars A, Ceccaldi M, Chepfer H, Clerbaux N, Cole J, Delanoë J, Domenech C, Donovan DP, Fukuda S, Hirakata M, Hogan RJ, Huenerbein A, Kollias P, Kubota T, Nakajima T, Nakajima TY, Nishizawa T, Ohno Y, Okamoto H, Oki R, Sato K, Satoh M, Shephard MW, Velázquez-Blázquez A, Wandinger U, Wehr T, van Zadelhoff G-J. 2015. The EarthCARE Satellite: The next step forward in global measurements of clouds, aerosols, precipitation and radiation. *Bull. Am. Meteorol. Soc.* **96**: 1311–1332.

Janisková M, Lopez P, Bauer P. 2012. Experimental 1D+4D-Var assimilation of CloudSat observations. *Q. J. R. Meteorol. Soc.* **138**: 1196–1220.

Kneifel S, Kollias P, Battaglia A, Leinonen J, Maahn M, Kaesle H, Tridon F. 2016. First observations of triple-frequency radar Doppler spectra in snowfall: Interpretation and applications. *Geophys. Res. Lett.* **43**: 2225–2233, doi: 10.1002/2015GL067618.

Leinonen J, Moisseev D, Nousiainen T. 2013. Linking snowflake microstructure to multi-frequency radar observations. *J. Geophys. Res.* **118**: 3259–3270, doi: 10.1002/jgrd.50163.

Lu Y, Clothiaux EE, Aydin K, Verlinde J. 2014. Estimating ice particle scattering properties using a modified Rayleigh–Gans approximation. *J. Geophys. Res.* **119**: 10471–10484, doi: 10.1002/2014JD021850.

Matrosov SY. 1992. Radar reflectivity in snowfall. *IEEE Trans. Geosci. Remote Sens.* **30**: 454–461.

Matrosov SY, Reinking RF, Kropfli RA, Bartram BW. 1996. Estimation of ice hydrometeor types and shapes from radar polarization measurements. *J. Atmos. Oceanic Technol.* **13**: 85–96.

Matrosov SY, Heymsfield AJ, Wang Z. 2005. Dual-frequency radar ratio of nonspherical atmospheric hydrometeors. *Geophys. Res. Lett.* **32**: L13816, doi: 10.1029/2005GL023210.

Nowell H, Liu G, Honeyager R. 2013. Modeling the microwave single-scattering properties of aggregate snowflakes. *J. Geophys. Res. Atmos.* **118**: 7873–7885, doi: 10.1002/jgrd.50620.

Petty GW, Huang W. 2010. Microwave backscatter and extinction by soft ice spheres and complex snow aggregates. *J. Atmos. Sci.* **67**: 769–787.

Seliga TA, Bringi VN. 1976. Potential use of radar differential reflectivity measurements at orthogonal polarizations for measuring precipitation. *J. Appl. Meteorol.* **15**: 69–76.

Sorensen CM. 2001. Light scattering by aggregates: A review. *Aerosol Sci. Technol.* **35**: 648–687.

Tiira J, Moisseev DN, von Lerber A, Ori D, Tokay A, Bliven LF, Petersen W. 2016. Ensemble mean density and its connection to other microphysical properties of falling snow as observed in Southern Finland. *Atmos. Meas. Tech.* **9**: 4825–4841, doi: 10.5194/amt-9-4825-2016.

Tyynelä J, Leinonen J, Moisseev D, Nousiainen T. 2011. Radar backscattering from snowflakes: Comparison of fractal, aggregate, and soft spheroid models. *J. Atmos. Oceanic Technol.* **28**: 1365–1372.

Tyynelä J, Leinonen J, Westbrook CD, Moisseev D, Nousiainen T. 2013. Applicability of the Rayleigh–Gans approximation for scattering by snowflakes at microwave frequencies in vertical incidence. *J. Geophys. Res.* **118**: 1826–1839, doi: 10.1002/jgrd.50167.

Um J, McFarquhar GM. 2007. Single-scattering properties of aggregates of bullet rosettes in cirrus. *J. Appl. Meteorol. Climatol.* **46**: 757–775.

Westbrook CD. 2014. Rayleigh scattering by hexagonal ice crystals and the interpretation of dual-polarisation radar measurements. *Q. J. R. Meteorol. Soc.* **140**: 2090–2096.

Westbrook CD, Ball RC, Field PR, Heymsfield AJ. 2004. Universality in snowflake formation. *Geophys. Res. Lett.* **31**: L15104, doi: 10.1029/2004GL020363.

Westbrook CD, Ball RC, Field PR. 2006. Radar scattering by aggregate snowflakes. *Q. J. R. Meteorol. Soc.* **132**: 897–914.

Yurkin MA, Hoekstra AG. 2011. The discrete-dipole-approximation code ADDA: Capabilities and known limitations. *J. Quant. Spectrosc. Radiat. Transfer* **112**: 2234–2247.